Publications

8-29-2018

Ultralow Frequency Electrodynamics of Magnetosphere-Ionosphere Interactions Near the Plasmapause During Substorms

Anatoly V. Streltsov
Embry Riddle Aeronautical University, streltsa@erau.edu

Evgeny V. Mishin
Air Force Research

Key Points:
- We explain large-scale and small-scale electric fields observed near the plasmapause
- Simulations reveal that the small-scale fields are produced by the ionospheric feedback mechanism
- We identify ionospheric parameters promoting development of the small-scale structures

Correspondence to:
A. V. Streltsov,
streltsa@erau.edu

Ultralow Frequency Electrodynamics of Magnetosphere-Ionosphere Interactions Near the Plasmapause During Substorms

Anatoly V. Streltsov[1,2] (iD) and **Evgeny V. Mishin[3]** (iD)

[1] Department of Physical Sciences, Embry-Riddle Aeronautical University, Daytona Beach, FL, USA, [2] National Academy of Sciences at Space Vehicles Directorate, Air Force Research Laboratory, Albuquerque, NM, USA, [3] Space Vehicles Directorate, Air Force Research, Albuquerque, NM, USA

Abstract Ultra low frequency (ULF) electromagnetic waves have been regularly observed by the CRRES, Cluster, and Van Allen Probes satellites near the plasmapause during substorms. Frequently, the small-scale waves are detected together with a large-scale quasi-stationary electric field collocating with mesoscale plasma flows penetrating into the plasmasphere. These observations suggest that the plasmapause plays an important role in the conversion of the kinetic energy of energetic particles moving toward the Earth from the reconnection site in the magnetotail into a large-scale electric field. The field penetrates along the magnetic field into the ionosphere and generates small-scale, shear Alfvén waves and field-aligned currents. These waves can form a standing pattern between the hemispheres, and under certain conditions, they can be amplified by interactions with the ionosphere. This scenario is verified in the paper by reproducing with simulations structure and amplitude of the ULF waves observed by the Van Allen Probe-A satellite near the plasmapause on 17 March 2015. The simulations are based on the reduced two-fluid MHD model describing generation of ULF Alfvén waves and field-aligned currents by the ionospheric feedback instability driven by the large-scale electric field. Simulations demonstrate good, quantitative agreement between spatial structure, frequency, and amplitude of the simulated waves and the observations.

1. Introduction

A proper description of the plasma and energy flows in the disturbed magnetosphere-ionosphere system is one of the critical steps in the modeling space weather. Its integral part is a transport of earthbound-ejected, mesoscale (hot) plasma flows or MPFs (Nishimura et al., 2014) through the magnetotail and penetration of the hot plasma into the plasmasphere leading to the enhanced ring current and subauroral ion drifts (SAID) and polarization streams (SAPS) (Mishin, 2013; Mishin et al., 2017, 2010). The plasmasphere boundary layer, aka plasmapause (Nishida, 1966), is a narrow region in the magnetosphere where the plasma density increases in the Earthward direction by a factor of 10–100 over the distance often as narrow as 50–100 km (Carpenter & Lemaire, 2004). It plays an important role in the transport of the hot plasma from the tail toward the Earth as indicated by the observations in the plasmasheric "hot zone" (Gringauz, 1983; Horwitz et al., 1986) and a good correlation of the locations of the plasmapause and the inner boundaries of the outer radiation belt (Foster et al., 2016; Goldstein et al., 2005; Li et al., 2006) and the plasma sheet (Mishin, 2013; Mishin et al., 2017). The latter, as well as the dispersionless character of the plasma sheet and aurora (Newell & Meng, 1987) boundaries, is well-explained in terms of a short-circuiting of MPFs near the plasmapause (Mishin, 2013; Mishin et al., 2010).

In brief, the low-ram pressure MPFs with the cross-tail width $<3\,R_E$ can propagate across the magnetic field due to the self-polarization field formed at the front of the hot (>1 keV) ion flow when the surrounding plasma cannot short out the polarization charge. The polarization shorting occurs when the cold plasma density exceeds 5–10 cm^{-3} (Mishin, 2013). As a result, the MPF's electron population stops, and the hot ions keep moving inward until being halted by the emerging outward electric field. The cold plasma maintains charge neutrality in the system, while enhanced plasma turbulence provides anomalous diffusion of the magnetic field and hot ions in the channel. Except for the turbulence and short-circuiting effects, a similar approach is used to understand impulsive plasma penetration into the dayside magnetopause (Gunell et al., 2012; Voitcu & Echim, 2016).
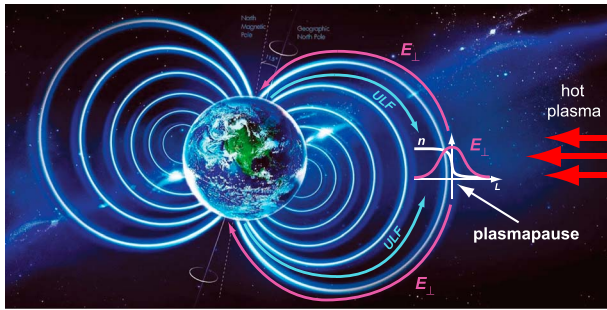
Figure 1. Schematic plot of the energy conversion on the plasmapause.

That scenario suggests that the plasmapause serves as a power plant in the magnetosphere, because the main goal of any power plant is to convert different types of energy into the electric energy. In this particular case the plasmapause converts kinetic energy of the hot MPF plasma into the energy of a large-scale (with the size of the order of the characteristic size of plasmasphere boundary layer) electric field. Such large-scale fields are frequently observed near the plasmapause together with small-scale (with the transverse size much less than the characteristic size of plasmasphere boundary layer) electromagnetic waves, especially during substorm breakups (Califf et al., 2016; Mishin & Burke, 2005; Mishin et al., 2017). For example, about 20 individual and storm-time substorm events consisting of crossing the plasmapause in less than 20–30 min after the onset of substorms by various satellites have been analyzed by Mishin et al., (2017 and references therein). The large-scale fields and small-scale waves have been observed in all duskside events. The low-altitude DMSP satellites observe such waves routinely equatorward of the substorm auroral boundary.

The in situ observations by the Cluster spacecrafts show that the quasi-static fields persist for more than 1–1.5 hr (Mishin, 2013; Mishin et al., 2017). This time is much greater than the transit time of the Alfvén waves between the hemispheres which is of the order a few minutes. The MPFs are the plasma jets in the magnetotail with the width across the tail less than 2–3 R_E, so that they occupy the magnetic local time region of ≈2 hr. The formation of the field on the duskside is not associated with gradient-curvature drift, which is too slow, but with the development of the substorm current wedge (Mishin et al., 2017). The maintenance of the field does not seem to require continuous impingement of MPF, at least for more than 30 min, the expansion phase duration.

ULF disturbances in the topside subauroral ionosphere composed of compressional and shear Alfvén waves are termed SAPS wave structures (Mishin et al., 2003). The small-scale oscillations decay in less than 1 hr after substorm onsets, while the large-scale fields (SAPS) remain for hours (Mishin & Burke, 2005). Considered among the most feasible mechanisms of SAPS wave structures are the ionospheric feedback instability (IFI; Streltsov & Lotko, 2004) and the current convective instability (Mishin & Burke, 2005).

This paper focuses on the connection between the large-scale, quasi-stationary electric field and small-scale ULF electric fields observed near the plasmapause by the Van Allen Probe-A satellite in the beginning of 17 March 2015 substorm (Mishin et al., 2017). We assume that the large-scale electric field appears near the plasmapause as a result of the short-circuiting mechanism. Once created in the equatorial magnetosphere, the electric field penetrates along the ambient magnetic field into the ionosphere and drives there the IFI. The IFI generates ULF waves that travel back and forth along the magnetic field between the hemispheres.

This concept is illustrated schematically in Figure 1, and the primary goal of this study is to verify it by reproducing structure and amplitude of the fields detected by the Van Allen Probes in the equatorial magnetosphere near the plasmapause with simulations of the two-fluid MHD model describing generation of ULF waves by the electric field in the ionosphere and propagation of these waves through the magnetosphere-ionosphere system.

2. Van Allen Probes 03/17/2015 Event

The observational event analyzed in this study was first published by Mishin et al. (2017), and it consists of large-amplitude variations of the electric field detected by the Van Allen Probe-A satellite in the equatorial magnetosphere during the time interval 07:33–08:11 UT on 17 March 2015 (hereafter, the 03/17/2015 event). It is illustrated in Figure 2, where Figure 2a shows the plasma density along the satellite trajectory, and Figure 2b shows V and H components of the measured electric field. In the *VDH* coordinate system, *V* is the radial/outward direction, *D* is the azimuthal/eastward direction, and *H* is the meridional/northward
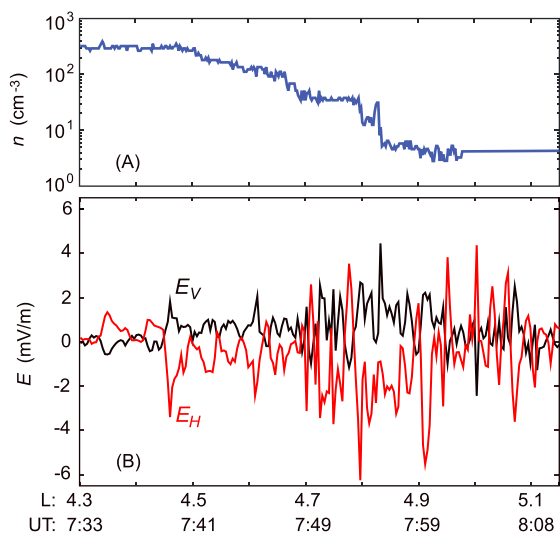

Figure 2. (a) Electron plasma density measured by the Van Allen Probes-A satellite during 07:33–08:11 UT on 15 March 2015 (the 03/17/2015 event). (b) V and H components of the electric field measured by the satellite during this event.
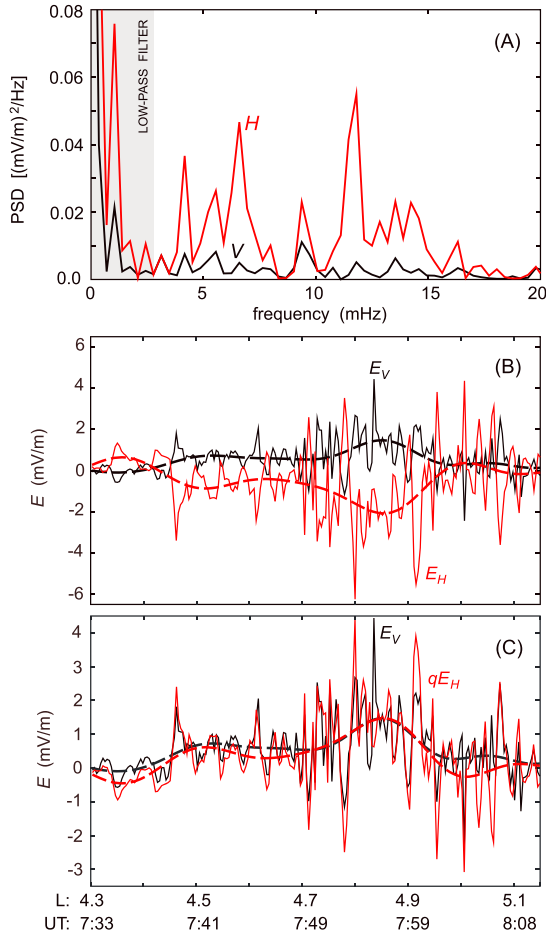
Figure 3. (a) Power spectral density (PSD) of E_H and E_V measured by the Van Allen Probes-A satellite during the 03/17/2015 event. The low-pass filter with a cutoff frequency 2.75 mHz is shown with a shaded rectangle. (b) Original E_H and E_V signals (solid lines) and the low-frequency parts of them, $E_{H_{LF}}$ and $E_{V_{LF}}$ (dashed lines). (c) The original E_V signal and the qE_V signal (here $q = \max(E_{V_{LF}})/\min(E_{H_{LF}})$).

direction. The spacecraft was moving between 20.3 and 20.6 hours of magnetic local time. The electric field components were obtained by transformation from GSE to VDH using ephemeris data. The **E** · **B** = 0 assumption is satisfied with accuracy better than 1%.

A more quantitative analysis of the electric fields shown in Figure 2b is illustrated in Figure 3. In particular, Figure 3a shows the power spectral density (PSD) of E_H and E_V. It also shows the low pass filter with a cutoff frequency ≈ 2.75 mHz (as a shaded rectangle) applied to E_H and E_V. Figure 3b shows the original signals (solid lines) and the low-frequency parts of them, $E_{H_{LF}}$ and $E_{V_{LF}}$ (dashed lines). Figure 3c shows the original E_V signal and the E_H signal multiplied by a coefficient $q = \max(E_{V_{LF}})/\min(E_{H_{LF}})$. Figure 3c demonstrates that all major peaks in the original E_H and E_V and in $E_{H_{LP}}$ and $E_{V_{LP}}$ are in phase. Which means that during the 03/17/2015 event, the satellite travels through a package of two-dimensional structures, consisting of ULF waves localized in the radial direction (or in the direction perpendicular to the dipole magnetic field) and extended in the azimuthal direction. The total magnitude of the low-frequency part of the electric field can be found as $E_{LF} = \sqrt{E_{H_{LF}}^2 + E_{V_{LF}}^2}$. This magnitude is plotted with a solid black line in Figure 4.

It is important to notice that during 03/17/2015 event, ULF waves had been observed for ≈ 38.5 min, and observations reveal many events similar to the one considered here. For example, Mishin et al. (2003), Mishin and Burke (2005), and Mishin et al. (2017) analyzed in detail the electric and magnetic variations in various events similar to the 03/17/2015 event in the ionosphere from DMSP satellites and in the magnetosphere from CRRES to show that such waves are indeed Alfvén waves. The phase relationship was found to be dependent of the frequency. That is, 0.1 – 1-Hz waves are propagating waves, while millihertz-range waves seem to be standing, as anticipated. These waves will be modeled with a two-fluid MHD model described in the next section.

3. Model

The two-fluid MHD model used in this study consists of the *magnetospheric* and *ionospheric* parts (Streltsov et al., 2012). The magnetospheric part considers the parallel motion of electrons and the perpendicular motion of ions in the dispersive Alfvén waves, and it consists of the electron parallel momentum equation, the density continuity equation, and the current continuity equation:

$$\frac{\partial v_{\|e}}{\partial t} + v_{\|e}\nabla_\| v_{\|e} + \frac{e}{m_e}E_\| + \frac{1}{m_e n_0}\nabla_\|\left(nT_e\right) = -v_e v_{\|e}, \tag{1}$$

$$\frac{\partial n}{\partial t} + \boldsymbol{\nabla}\cdot\left(n v_{\|e}\hat{\mathbf{b}}\right) = 0, \tag{2}$$

$$\boldsymbol{\nabla}\cdot j_\|\hat{\mathbf{b}} + \frac{1}{\mu_0}\boldsymbol{\nabla}\cdot\left(\frac{1}{c^2} + \frac{1}{v_A^2}\right)\frac{\partial \mathbf{E}_\perp}{\partial t} = 0. \tag{3}$$

Here the subscripts $\|$ and $\perp$ denote vector components in the directions parallel and perpendicular to $\hat{\mathbf{b}} = \boldsymbol{B}_0/B_0$, respectively; $v_{\|e}$ is the parallel component of the electron velocity; T_e is the background electron temperature, c is the speed of light; $v_A = B_0/\sqrt{\mu_0 n_0 m_i}$ is the Alfvén speed; and v_e is the electron collision frequency. At low altitudes, plasma mostly consists of heavy ions (O_2^+ and NO^+), and the ion mass is modeled as $m_i = m_p\left(1 + 31e^{-((r-r_1)/r_0)^2}\right)$, where m_p is the proton mass, $r_1 = 110.0/R_E$, and $r_0 = 600.0/R_E$ (Streltsov & Lotko, 2004).

Since the analysis of 03/17/2015 event illustrated in Figure 3 reveals predominantly two-dimensional structure of the observed fields, equations(1)–(3) are implemented numerically in a two-dimensional, axisymmetric
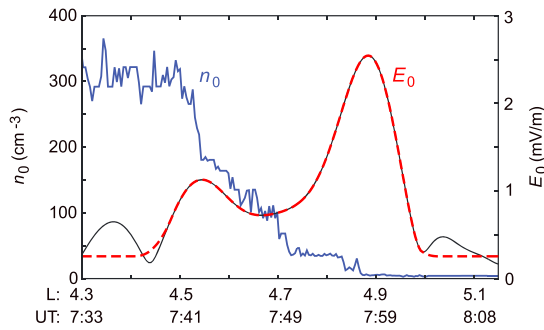
Figure 4. The solid black line shows the magnitude of the electric field measured during the 03/17/2015 event. The red-dashed line shows the magnitude of the electric field used to construct a background electric field inside the computational domain. The solid blue line shows the magnitude of the background plasma density used in the simulations in the equatorial region.

dipole magnetic field geometry. The finite-difference time-domain technique is used to approximate the partial derivatives in (1)–(3), and the fourth-order predictor-corrector methods based on the Adams-Bashforth numerical scheme is used to advance the model in time (Streltsov et al., 2012).

The computational domain represents a 2-D slice of the dipole magnetic field bounded by $L_1 = 4.30$ and $L_2 = 5.15$ magnetic shells. The ionospheric boundaries of the domain are set at 110-km altitude. There the ionospheric part of the model describes interactions between the field-aligned currents carried by ULF Alfvén waves and plasma in the E region. The key aspect of these interactions is the active ionospheric feedback of the density disturbances caused by field-aligned currents on structure and amplitude of these field-aligned currents.

The ionospheric feedback mechanism has been extensively studied at high latitudes for more than 40 years (e.g., Atkinson, 1970; Lysak, 1991; Lysak & Song, 2002; Miura & Sato, 1980; Pokhotelov et al., 2000; Russell et al., 2013; Sato, 1978; Streltsov & Lotko, 2004, 2005; Trakhtengertz & Feldstein, 1981, 1991; Watanabe et al., 1993). These studies demonstrate that under favorable conditions, the feedback can work in a constructive way, leading to the IFI, which can generate intense, small-scale field-aligned currents and density structures in the E region. The favorable conditions for IFI development include the large-scale electric field and the low ionospheric density in the E region. The electric field provides the energy for the intensification of the small-scale ULF waves and field-aligned currents due to the so-called *over reflection* from the ionosphere (e.g., Lysak & Song, 2002). The low ionospheric density (a) provides a low conductance of the E region, which allows the electric field generated in the equatorial magnetosphere to penetrate into the ionosphere, and (b) reduces the effects of the recombination, which saturate the instability.

Because the height of the conducting portion of the ionosphere is much less than the parallel wavelength of ULF waves, it can be considered as a narrow slab, where the density and the electric field are relatively uniform. In that case, the simplest mathematical form of the ionospheric part of the model can be given by two equations connecting the perpendicular electric field, $E_\perp$, and the plasma density, n_E, in the ionosphere with the field-aligned current density, $j_\parallel$. One is the Poisson equation, derived by integrating the current continuity equation $\nabla \cdot j = 0$ over the effective thickness of the ionospheric E region ($h \approx 20$ km):

$$\nabla \cdot (\Sigma_P \mathbf{E}_\perp) = \pm j_\parallel. \tag{4}$$

Another is the ionospheric density continuity equation:

$$\frac{\partial n_E}{\partial t} = \frac{j_\parallel}{eh} + \alpha n_E^2 - \alpha n_{E0}^2. \tag{5}$$

Here $\Sigma_P = M_P n_E h e / \cos \psi$; $M_P = 10^4$ m²/sV is the ion Pedersen mobility (the Hall conductivity is not included in (4) due to the two-dimensionality of the considered problem); e is the elementary charge; ψ is the angle between the normal to the ionosphere, and $L = 4.9$ dipole magnetic field line at 100-km altitude. In (4) the "+" sign is used in the southern hemisphere, and the "-" sign is used in the northern hemisphere. The term αn_E^2 in the right-hand side of (5) represents losses due to the recombination ($\alpha = 3 \times 10^{-7}$ cm³/s is the coefficient of recombination); and the term αn_{0E}^2 represents the unperturbed source of the ionospheric plasma providing an equilibrium state of the ionosphere, n_{E0}.

The assumption that the ionospheric E region is a narrow conducting slab described with equations (4) and (5) substantially simplifies the model. The ionospheric part of the model can be made more sophisticated by including various physical mechanisms. For example, it may include effects of the neutral winds and the effects of the inhomogeneity with altitude of the ion-neutral collision frequency in the ionospheric E region. Inclusion of these effects will make the boundary conditions more complex and require more assumptions about various ionospheric parameters (because the direct measurements may not be conducted in the "right" place in the ionosphere when some events-of-interest are observed on satellites in the magnetosphere), but, what is very important, they do not change the basic physics of the ionospheric feedback interactions.
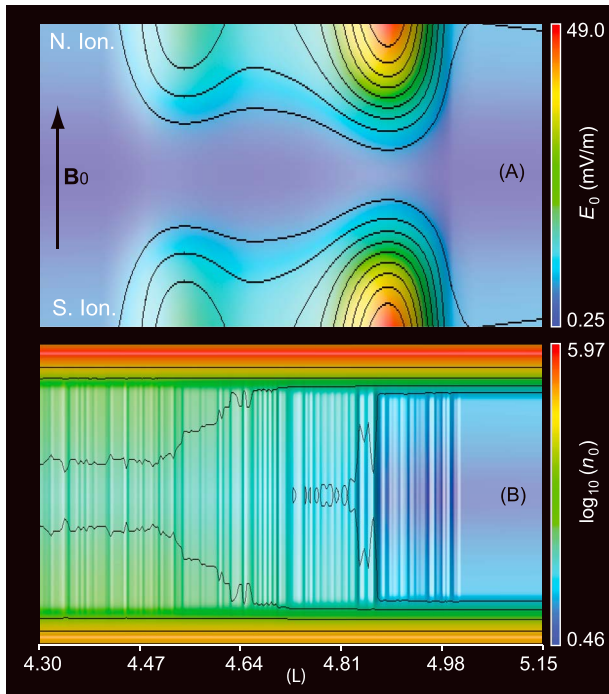
Figure 5. (a) The background electric field and (b) the electron plasma density inside the computational domain.

For example, Sydorenko and Rankin (2017) suggested that the inhomogeneity with the altitude of the ion-neutral collision frequency can saturate IFI development or even prevent it from occurring because it creates a shear in the ion velocity at low altitudes which can "smooth out" the localized disturbances of the ionospheric conductivity which are an important part of IFI. However, this particular effect had been carefully investigated by Trakhtengertz and Feldstein (1981, 1984, 1991), who demonstrated that this inhomogeneity can change the threshold and the growth rate of the instability, but it certainly does not prevent its occurrence when the magnitude of the electric field in the ionosphere exceeds the threshold value. The ionospheric feedback boundary conditions for the model including effects of the altitude-dependence of the ion-neutral collision frequency are given by equations (A6)–(A11) in Trakhtengertz and Feldstein (1991). These equations demonstrate that the effect of the inhomogeneity of the collision frequency with altitude strongly depends on the density profile in the ionosphere, and the more the conductivity is localized in the narrow region, the less important this effect is.

The nighttime density and conductivity profiles below the ionospheric F region are given by Titheridge (2003). These profiles demonstrate that during the nighttime, the density in the ionosphere is low, and the Pedersen conductivity indeed is concentrated in the narrow slab with $\approx 10-20$-km effective height. In this case effects of velocity shear are not important for the development of IFI, and the active ionospheric response on the magnetospheric field-aligned current in ULF frequency range can be adequately described with equations (4) and (5)

3.1. Background Parameters

The main background parameters defining spatial structure, amplitude, and dynamics of ULF waves in the numerical model are the magnetic field, electric field, and plasma density. The background magnetic field is assumed to be a dipole: $B_0 = B_* (1 + 3 \sin^2 \theta)^{1/2}/r^3$, where $B_* = 31.000$ nT; θ is the magnetic latitude; and r is a geocentric distance measured in $R_E = 6,371.2$ km. The dipole magnetic field is a reasonable approximation of the background field near the plasmapause ($L = 4.5 - 4.9$), and we do not expect that our results will change qualitatively if a more realistic model for the magnetic field will be used.

The background electric field, $\mathbf{E}_{\perp 0}$, is defined from the low-frequency part of the field measured by the Van Allen Probe-A satellite during the 03/17/2015 event. This field is measured in the equatorial magnetosphere, and it is shown with the red-dashed curve in Figure 4. The electric field inside the entire domain is constructed in two steps. In the first step, the field shown in Figure 4 is integrated in the direction perpendicular to the background magnetic field to get the electric potential, ϕ, in the equatorial magnetosphere. In the second step, this potential is mapped equiv-potentially along the ambient magnetic field through the entire domain, and the background electric field is calculated as $\mathbf{E}_{\perp 0} = -\nabla_\perp \phi$ everywhere. The 2-D plot of the resulting electric field is shown in Figure 5a.

The background plasma density in the domain is constructed using data from 03/17/2015 event and the information about the background electric field. We consider a general case when the ionospheric plasma densities in the southern and northern hemispheres are not equal to each other. The density in each hemisphere is given with the formula

$$n_0(L, \mu) = \begin{cases} n_{1_{N,S}}(L)(r - r_2) + n_{2_{N,S}}(L), & r_1 < r < r_2 \\ n_{3_{N,S}}(L) e^{-(r-r_2)/r_0} + n_{4_{N,S}}(L)/r, & r > r_2 \end{cases}. \tag{6}$$

Here $r = r(L, \mu)$ is the geocentric distance to the point with the dipole coordinates L and μ; $r_0 = 0.0175$; $r_1 = 1 + 110/R_E$ (near the E region maximum); $r_2 = 1 + 270/R_E$ (near the F region maximum); and the functions $n_{1_{N,S}}(L)$, $n_{2_{N,S}}(L)$, $n_{3_{N,S}}(L)$, and $n_{4_{N,S}}(L)$ define densities in the ionospheric E region, F region, and in the equatorial magnetosphere. In particular, $n_{4_N}(L) \equiv n_{4_S}(L)$ is chosen to provide the density profile in the equatorial magnetosphere shown in Figure 4. Function $n_{2_S}(L)$ is chosen to provide a density magnitude of
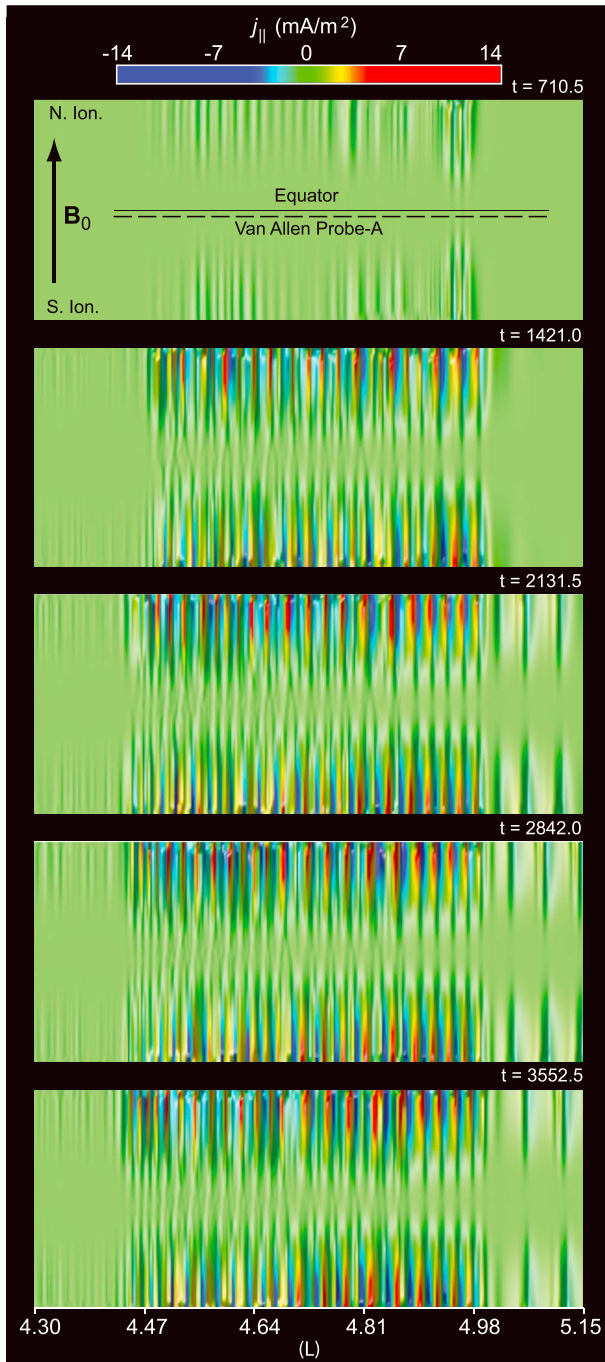
Figure 6. Five snapshots of the parallel current density in the magnetosphere taken from the simulation.

2.0×10^5 cm^{-3} in the southern F region, and $n_{2_N}(L)$ is chosen to provide a density of 1.0×10^6 cm^{-3} in the northern F region. The factor of 10 differences in the ionospheric density between the northern and southern hemispheres is very typical for the situation when one hemisphere is in the night and another is in the day light, which happens quite frequently. Both values of the ionospheric density are well within the range of the observational values.

Function $n_{1_{N,S}}(L)$ is chosen from a current-free equilibrium state: They both are inversely proportional to $E_{\perp 0}$ in the ionosphere, so that $\nabla \cdot (\Sigma_{P_{N,S}} \mathbf{E}_{0\perp}) = 0$. But the constants of proportionality between $E_{\perp 0}$ and $n_{1_{N,S}}(L)$ are different in the southern and northern hemispheres: In particular, $n_{1_N}(L)$ provides a minimum density in the northern E region of 5.0×10^4 cm^{-3}, and $n_{1_S}(L)$ provides a minimum density in the southern E region of 1.0×10^4 cm^{-3}. The resulting 2-D plot of $\log_{10}(n_0)$ inside the computational domain is shown in Figure 5b.

The current-free relation between E_0 and n_0 used in this study is observed in the subauroral ionosphere by the low-orbiting satellites and ground-based radars (e.g., Foster & Burke, 2002; Mishin et al., 2003). This current-free equilibrium state is an important feature of the considered events, because the main hypothesis investigated here is that the ULF waves are generated by the electric field in the ionosphere, and these waves are observed for an extended period of time. For example, in the 03/17/2015 event, the ULF waves are observed during $\approx$38.50 min, which means that the electric field in the ionosphere exists at least during that time. If this field is not in the current-free equilibrium with the density/conductivity in the ionosphere, then it will generate there a large-scale field-aligned currents which will produce the electric field with the opposite polarity diminishing the original field.

4. Results and Discussion

In this section we summarize the results from a large number of simulations and chose for illustration purposes only the results matching the 03/17/2015 observations in most detail. Thus, Figure 6 shows five snapshots of the parallel current density taken from the simulation at $t = 710.5$, 1,421.0, 2,131.5, 2,842.0, and 3,552.5 s. The red color marks "positive" field-aligned currents flowing in the direction of the ambient magnetic field (from the southern to northern hemispheres), and the blue color marks "negative" field-aligned currents flowing in the opposite direction. The simulations were conducted for the minimum value of the E region density in the southern hemisphere of $n_{ES} = 1.0 \times 10^4$ cm^{-3} (corresponds to $\Sigma_P = 0.32$ mho) and the minimum value of the E region density in the northern hemisphere of $n_{EN} = 5.0 \times 10^4$ cm^{-3} (corresponds to $\Sigma_P = 1.60$ mho). The density value in the F peak is $n_{FS} = 2.0 \times 10^5$ cm^{-3} and $n_{FN} = 1.0 \times 10^6$ cm^{-3} in the southern hemisphere and $n_{FN} = 1.0 \times 10^6$ cm^{-3} in the northern. The background electric field has the maximum amplitude of 49 mV/m on the ionosphere in both hemispheres. The two dimensional plots of the magnitude of the background electric field and density inside the computational domain are shown in Figure 5.

This particular set of parameters had been chosen from several runs of simulations as the ones providing the best correlation between the numerical results and the 03/17/2015 observations. For example, numerical results similar to the one discussed in the paper were obtained in the simulations with (1) $n_{ES} = 0.25 \times 10^4$ cm^{-3}, $n_{EN} = 5.0 \times 10^4$ cm^{-3}, $n_{FS} = 1.0 \times 10^5$ cm^{-3}, and $n_{FN} = 1.0 \times 10^6$ cm^{-3}; (2) $n_{ES} = 0.5 \times 10^4$ cm^{-3}, $n_{EN} = 5.0 \times 10^4$ cm^{-3}, $n_{FS} = 1.0 \times 10^5$ cm^{-3}, and $n_{FN} = 1.0 \times 10^6$ cm^{-3}; and (3) $n_{ES} = 2.0 \times 10^4$ cm^{-3}, $n_{EN} = 6.0 \times 10^4$ cm^{-3}, $n_{FS} = 2.0 \times 10^5$ cm^{-3}; and $n_{FN} = 6.0 \times 10^5$ cm^{-3}.
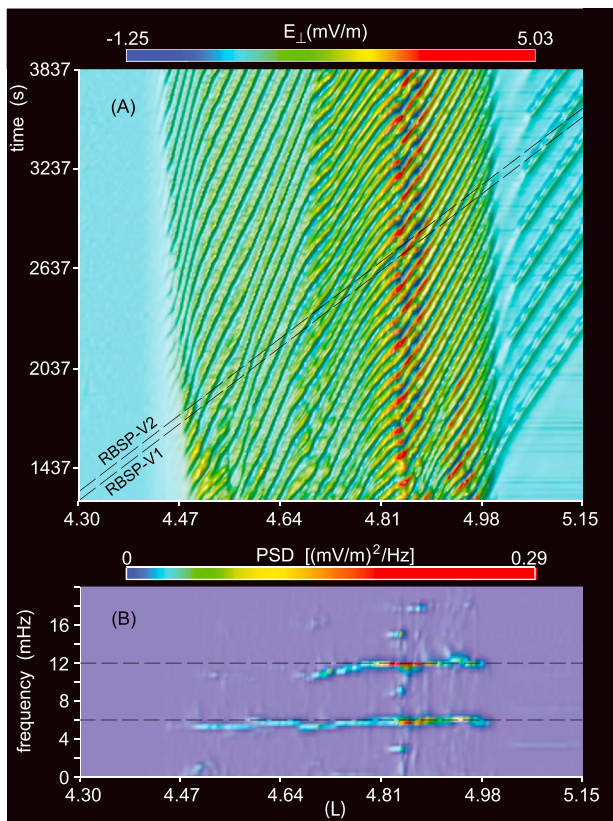
Figure 7. (a) Temporal dynamics and spatial structure of the simulated perpendicular electric field along the trajectory of the RBSP-A satellite in the magnetosphere during the 03/17/2015 event. Two dashed lines marks two space-time "trajectories" of virtual satellites RBSP-V1 and RBSP-V2 "flying" through the computational domain in different moments of time. (b) Power spectral density (PSD) in the frequency range 0–20 mHz of the electric field shown in (a). RBSP = Van Allen Probes (aka Radiation Belt Storm Probes).

There are two particular features of these parameters worth to be discussed. The first one is a relatively low ionospheric density/conductivity to the nighttime conditions at least in one hemisphere. The low state of the ionospheric conductivity is an important necessary condition for the development of the instability. When the conductivity is high, the instability can be suppressed by the recombination in the E region, which is proportional to the αn_0^2 (Miura & Sato, 1980; Streltsov & Lotko, 2005), and such suppression had been observed in several simulations conducted with a relatively high ionospheric density. It should be mentioned here that the instability can develop even in the high-density/conductivity case, but it will require much larger magnitude of the electric field than it is observed during 03/17/2015 event.

Another important feature of these parameters is the asymmetry between the ionospheric density/conductivity in two hemispheres. It has been shown by Pokhotelov et al. (2002) that such asymmetry causes asymmetry in amplitude of electric fields and currents produced by standing Alfvén waves in southern and northern hemispheres. The electric field has larger magnitude in the hemisphere with a smaller ionospheric conductivity, and the field-aligned current has smaller amplitude in this hemisphere. This effect is a direct consequence of how the electromagnetic waves reflect from a surface with a finite conductivity. The practical importance of this asymmetry for modeling 03/17/2015 event is that during this event, the satellite crosses the magnetic field lines near the magnetic equator. (The trajectory of the Van Allen Probe-A satellite along the magnetic latitude $\theta \approx -12°$ mapped into the computational domain is shown with a dashed line in the top frame in Figure 6.) And if the ionospheric densities/conductivities are identical in both hemispheres, then the structure of standing ULF waves will be symmetrical relative to the equator with minimum in the electric field and field-aligned currents in the equatorial region. Thus, different density magnitudes in two hemispheres provide different magnitudes of the small-scale electric fields near the equator for the same magnitude of the large-scale electric field. We define a "large-scale" structure as the structure with the size larger then or equal to the size of the plasmapause, (≈ 0.5 L, see Figure 4), and a "small-scale" structure as the structure with the size much less than the size of the plasmapause (see Figure 6).

In the simulation illustrated in Figure 6, the development of the small-scale currents produced by the IFI has been triggered by the numerical noise which can be interpreted as a random thermal fluctuations of plasma density in the real ionosphere. The top panel in Figure 6 shows that the small-scale structures start to develop almost in the entire region where the electric field exceeds the threshold amplitude for the instability. Four other panels in Figure 6 show that during the time interval from 1,421 to 3,552.5 s, the instability reaches saturated states, and it produces small-scale ULF waves with almost constant amplitudes and spatial scales within the same spatial region bounded by $L \approx 4.45$ and $L \approx 5.00$.

These effects are illustrated in more detail in Figure 7. Figure 7a shows the temporal dynamics and spatial structure of the perpendicular electric field taken from the simulation along the the trajectory of the Van Allen Probe-A satellite mapped into the computational domain. (It is shown with the dashed line marked as Radiation Belt Storm Probes (RBSP)-A in the top panel in Figure 6.) The bottom panel (Figure 7b) shows spatial structure of the PSD in the range 0–20 mHz of the electric field shown in Figure 7a. Figure 7b again emphasizes the fact that the instability produces small-scale electromagnetic waves with almost constant frequencies and spatial scales localized in some particular region in space and lasting for more than 40 min. The frequencies of these waves are 6 mHz and 12 nHz.

To make a detailed comparison between the numerical results and the 03/17/2015 observations, two virtual satellites, RBSP-V1 and RBSP-V2, were "flying" through the simulation along the trajectory and with the velocity corresponding to the real Van Allen Probe-A satellite. The virtual trajectory was chosen to be perpendicular
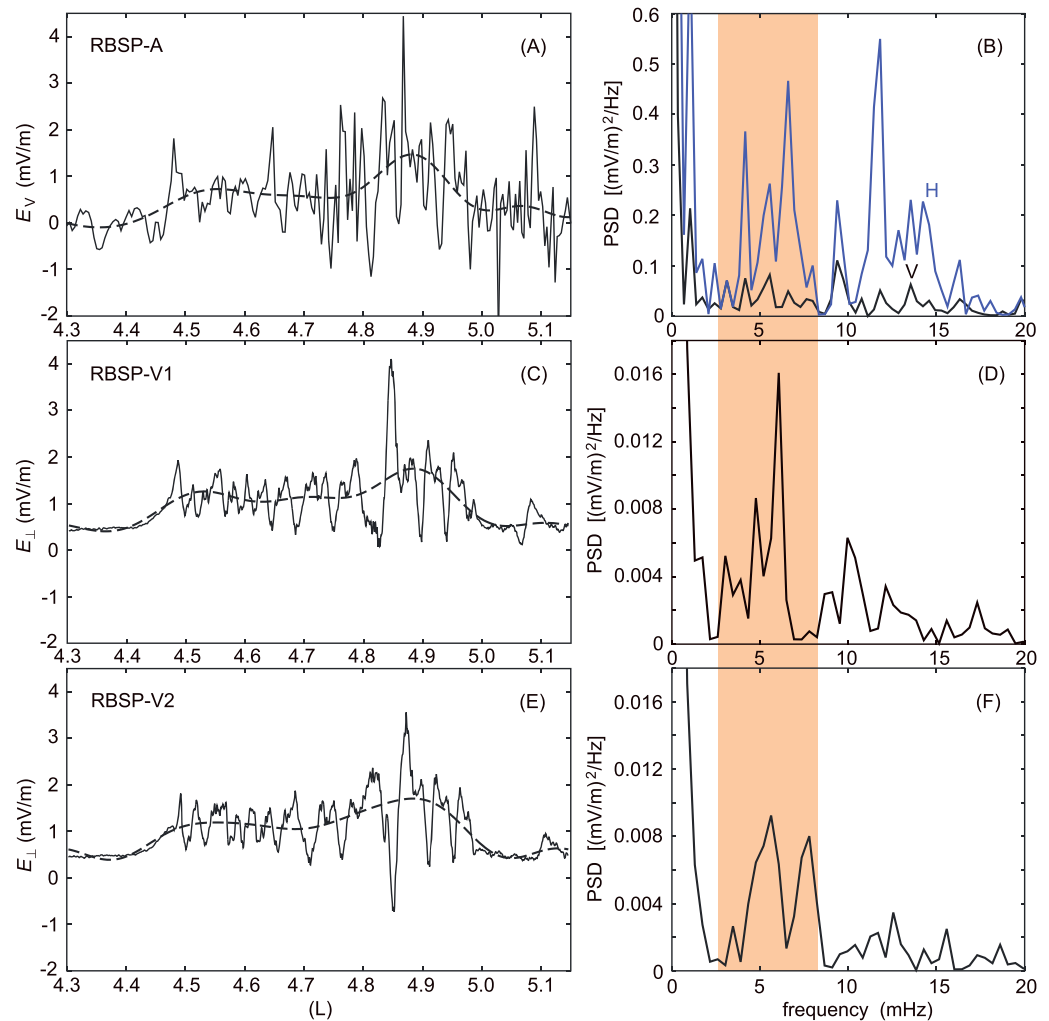
Figure 8. (a) V component of the perpendicular electric field observed during 03/17/2015 event. (b) Power spectral density (PSD) in the frequency range 0–20 mHz of V and H components of the electric field observed during the 03/17/2015 event. (c and e) Perpendicular electric field "measured" by the RBSP-V1 and RBSP-V2 satellites. (d and f) PSD in the frequency range 0–20 mHz of the electric field measured by the RBSP-V1 and RBSP-V2 satellites.

to the background dipole magnetic field near the magnetic latitude $\theta = -12°$. The velocity of the satellite had been estimated from the 03/17/2015 observations showing that the Van Allen Probe-A satellite travels from $L = 4.30$ to $L = 5.15$ in ≈ 38.5 min, which gives the satellite speed 3.68×10^{-4} L/s or 2.34 km/s in the equatorial magnetosphere. Navigational data of the Van Allen Probe-A satellite show that during the 03/17/2015 event, the L component of the satellite velocity was not uniform, but the difference between the real velocity and the estimated value is insignificantly small. Therefore, the trajectories of the virtual satellites are shown with two straight, dashed lines in the time-space domain illustrated in Figure 7a. Two trajectories were chosen to illustrate the difference in the structure of measured ULF waves depending on the time when the satellite crosses the plasmapause.

The comparison between the numerical results and the observations is shown in Figure 8. Figure 8a shows E_V measured by the Van Allen Probe-A satellite during the 03/17/2015 event with a solid black line. The low-frequency part of the signal is shown with a dashed line. It should be reminded here that the structure of E_V and E_H observed during 03/17/2015 event is very similar (see Figure 3c), and this is the reason to show only E_V in Figure 8a. Figure 8b shows the PSDs of the measured E_V and E_H in a frequency range 0–20 mHz. Figures 8c and 8e show the perpendicular electric field, E_L, taken from the simulation along the virtual "trajectories" RBSP-V1 and RBSP-V2. Figures 8d and 8f show the PSDs of the fields shown in Figures 8c and 8e

correspondingly. The main conclusion from Figure 8 is that the numerical results demonstrate good, quantitative agreement with the waves observed in the magnetosphere near the plasmapause. In particular, the amplitudes, location, and the spatial structures of the simulated waves match observations quite well. The PSDs of the measured and simulated fields also show good correlations, particularly in the frequency range 3–8 mHz, which may corresponds to the first dominant frequency obtained in the simulation of 6 mHz. PSDs of the observed and simulated fields in Figures 8b, 8d, and 8e also shows some peaks in the frequency range 10–13 mHz, which may correspond the second dominant frequency obtained in the simulation of 12 mHz. The high degree of correlation between the numerical results and observations let us conclude that the model of the ionospheric feedback interactions considered in this study adequately represents the basic physics of the magnetosphere-ionosphere (MI) coupling carried by ULF waves and field-aligned currents.

Our simulations demonstrate that the presented model can produce a broad range of small-scale ULF waves/structures with different amplitudes, frequencies, and spatial scales depending on the background parameters. However, the model has its own limitations which should be discussed as well. The two major parameters of this model is the background electric field and the plasma density in the ionospheric E region. The field serves as the constant source of the free energy for the generation of small-scale electric fields and currents by IFI, but the model does not explain what physical mechanism produces this electric field. To provide the long-lasting generation of the ULF waves by the ionospheric feedback, the field should be in the current-free equilibrium with the ionospheric density/conductivity. If this condition is not satisfied, this field will generate large-scale field-aligned currents in the ionosphere, and these currents will travel with the Alfvén velocity between the hemispheres, and the entire magnetosphere-ionosphere system will oscillate with some ULF frequency. These oscillations are not detected neither in the observations nor in the simulation. Therefore, the model does not describe the transition process when the electric field and the plasma density in the ionosphere reaches some equilibrium state.

One such transition process had been successfully modeled with the same set of equations for ULF waves/field-aligned currents in the magnetosphere and the active ionospheric feedback as the one considered in this study by Streltsov and Lotko (2005); however, the main difference between that work and the present study is the presence of the large-scale field-aligned current interacting with the ionosphere at high altitudes in Streltsov and Lotko (2005). That field-aligned currents self-consistently cause the electric field in the ionosphere and modify the ionospheric density accordingly. That approach is suitable for the open/extended magnetic field lines mapping the auroral ionosphere into the distant tail, but it is not applicable to the subauroral zone, near the plasmapause, where the magnetic field lines are closed.

Another physical mechanism considered in the literature to explain excitation of the large-scale electric field in the magnetosphere is the field line resonance. It is produced by the standing shear Alfvén waves and can be driven by the compressible, fast MHD modes, propagating across the magnetic field from the magnetotail (Samson et al., 1992; Southwood, 1974) or by the incompressible, large-scale surface waves (Hasegawa, 1976; Streltsov & Lotko, 1995). The transverse gradient in the magnetospheric plasma is important for the excitation of field line resonance by both mechanisms. It promotes coupling between fast and intermediate MHD modes in the first case and development of the surface waves on the sharp density gradients in the second case. Both of these mechanisms were not applicable to the 03/17/2015 event because in order to excite field line resonance, the driver (and the large-scale field) must oscillate with the eigenfrequency of the resonator. But the observations of the 03/17/2015 event (and several other similar events reported by Mishin et al., 2017) demonstrate that the large-scale electric field is quasi-static, at least during the time of the event ($\geq$40 min).

Therefore, the most suitable mechanism for the explanation of the large-scale electric field in the magnetosphere is the injection of the hot plasma from the reconnection site in the magnetotail into the inner magnetosphere and the interactions between hot particles and the cold plasma inside the plasmasphere. This process, investigated by Mishin et al. (2010), Mishin (2013), and Mishin et al. (2017), suggests that the relatively cold and dense electrons inside the plasmasphere "short cut" the electric current carried by the hot electrons, and the hot ions transport the positive charge further inside the plasmasphere then the hot electrons can transport negative charge. As a result, a large-scale electric field pointed in the outward from the Earth direction is generated near the plasmapause by the hot ions penetrating inside the plasmasphere further than the hot electrons. The magnitude and polarity of this field correspond to the parameters of the field observed during 03/17/2015 event.

Therefore, the plasmapause in the short cut mechanism acts as a boundary for the hot electrons injected from the magnetotail, and consequently, it defines the location where the large-scale perpendicular electric field is generated in the magnetosphere. In other words, one can say that plasmapause serves as a power plant in the magnetosphere, because the main goal of any power plant is to convert different types of energy into the electric energy. The small-scale waves are produced by the IFI in the ionosphere, and their parameters (frequency and the perpendicular wavelength) are defined mostly by the parameters of the ionosphere. This can be seen from the frequencies of the ULF waves illustrated in Figure 7b. In particular, the main dominant frequency of the ULF waves obtained in the simulations changes very little in the region between $L = 4.47$ and $L = 4.98$, whereas the plasma density in the equatorial magnetosphere changes there almost by a factor of 100 (which means that the local Alfvén speed changes by a factor of 10).

5. Conclusions

The results from this numerical study demonstrate that the small-scale electromagnetic waves frequently observed by satellites in the equatorial magnetosphere in the vicinity of the plasma pause can be generated by the magnetosphere-ionosphere interactions carried by the ULF field-aligned currents in the subauroral zone. These currents are produced by the IFI driven by the large-scale electric field in the ionosphere. This quasi-stationary field is generated in the equatorial magnetosphere by the interactions between the hot, tenuous particles injected into the inner magnetosphere from the reconnection site in the magnetotail and the cold, dense plasma inside the plasmasphere. The field is mapped electro-statically along the geomagnetic field into the ionosphere in both hemispheres.

This theoretical concept has been used to explain observations performed by the Van Allen Probe-A satellite in the equatorial magnetosphere at the radial distance $\approx 5\ R_E$ on 17 March 2015. The observations reveal small-scale, two-dimensional electromagnetic waves accompanied by the large-scale electric field in the vicinity of the strong transverse gradient in the plasma density (aka plasmapause). The observations have been modeled with the two-fluid MHD code, describing propagation of the ULF waves and field-aligned currents in the magnetosphere and interactions between these currents and the ionospheric plasma. In particular, the model includes effects of the active ionospheric feedback on structure and amplitude of the currents causing variation in the ionospheric density/conductivity.

Simulations demonstrate that for the magnitude and structure of the large-scale electric field observed during the 03/17/2015 event, the IFI develops when the conductivity in at least one of the hemispheres is relatively low ($\Sigma_P = 0.32$ mho). The instability produces ULF waves with frequencies and perpendicular sizes matching the observations in good, quantitative detail. In particular, numerical results match observations in the wave frequency, amplitude, and the perpendicular wavelength. The simulations also show that the instability develops in the localized region in the ionosphere where the necessary conditions for it are satisfied, and it reaches some dynamic steady-state which can last for more than 40 min. This last finding explains the fact that these waves are observed in the vicinity of the plasma pause quite frequently.

6. Data Availability

The electric field and density measured by the Van Allen Probe-A satellite during 07:33–08:11 UT on 17 March and shown in Figure 2, the executable code used in the simulations, the data files used to run the code, and the results from the simulation shown in Figure 6 are available from Figshare.com (https://doi.org/10.6084/m9.figshare.6823091.v1).

References

Atkinson, G. (1970). Auroral arcs: Result of the interaction of a dynamic magnetosphere with the ionosphere. *Journal of Geophysical Research*, *75*, 4746–4755.

Califf, S., Li, X., Wolf, R., Zhao, H., Jaynes, A., Wilder, F., et al. (2016). Large-amplitude electric fields in the inner magnetosphere: Van Allen Probes observations of subauroral polarization streams. *Journal of Geophysical Research: Space Physics*, *121*, 5294–5306. https://doi.org/10.1002/2015JA022252

Carpenter, D. L., & Lemaire, J. (2004). The plasmasphere boundary layer. *Annales de Geophysique*, *22*, 4291–4298. https://doi.org/10.5194/angeo-22-4291-2004

Foster, J. C., & Burke, W. J. (2002). SAPS: A new categorization for sub-auroral electric fields. *EOS*, *83*, 393–394.

Foster, J., Erickson, P., Baker, D., Jaynes, A., Mishin, E., Fennel, J., et al. (2016). Observations of the impenetrable barrier, the plasmapause, and the VLF bubble during the 17 March 2015 storm. *Journal of Geophysical Research: Space Physics*, *121*, 5537–5548. https://doi.org/10.1002/2016JA022509

Goldstein, J., Kanekal, S., Baker, D., & Sandel, B. (2005). Dynamic relationship between the outer radiation belt and the plasmapause during March–May 2001. *Geophysical Research Letters*, *32*, L15104. https://doi.org/10.1029/2005GL023431

Gringauz, K. (1983). Plasmasphere and its interaction with the ring current. *Journal of Geophysical Research*, *34*, 245–257.

Gunell, H., Nilsson, H., Stenberg, G., Hamrin, M., Karlsson, T., Maggiolo, R., et al. (2012). Ionospheric heating at Arecibo: First tests. *Physics of Plasmas*, *19*, 072906. https://doi.org/10.1063/1.4739446

Hasegawa, A. (1976). Particle acceleration by MHD surface wave and formation of aurora. *Journal of Geophysical Research*, *81*, 5083–5090.

Horwitz, J., Comfort, R., & Chappell, C. (1986). Plasmasphere and plasmapause region characteristics as measured by DE-1. *Advances in Space Research*, *6*, 21. https://doi.org/10.1016/0273-1177(86)90313-3

Li, X., Baker, D., O'Brien, T., Xie, L., & Zong, Q. (2006). Correlation between the inner edge of outer radiation belt electrons and the innermost plasmapause location. *Geophysical Research Letters*, *33*, L14107. https://doi.org/10.1029/2006GL026294

Lysak, R. L. (1991). Feedback instability of the ionospheric resonant cavity. *Journal of Geophysical Research*, *96*, 1553.

Lysak, R. L., & Song, Y. (2002). Energetics of the ionospheric feedback interaction. *Journal of Geophysical Research*, *107*(A8), 1160. https://doi.org/10.1029/2001JA000308

Mishin, E. V. (2013). Interaction of substorm injections with the subauroral geospace: 1. Multispacecraft observations of SAID. *Journal of Geophysical Research: Space Physics*, *118*, 5782–5796. https://doi.org/10.1002/jgra.50548

Mishin, E. V., & Burke, W. J. (2005). Stormtime coupling of the ring current, plasmasphere and topside ionosphere: Electromagnetic and plasma disturbances. *Journal of Geophysical Research*, *110*, A07209. https://doi.org/10.1029/2005JA011021

Mishin, E. V., Burke, W. J., Huang, C. Y., & Rich, F. J. (2003). Electromagnetic wave structures within sub-auroral polarization streams. *Journal of Geophysical Research*, *108*, 1309. https://doi.org/10.1029/2002JA009793

Mishin, E. V., Nishimura, Y., & Foster, J. (2017). SAPS/SAID revisited: A causal relation to the substorm current wedge. *Journal of Geophysical Research: Space Physics*, *122*, 8516–8535. https://doi.org/10.1002/2017JA024263

Mishin, E., Puhl-Quinn, P., & Santolik, O. (2010). SAID: A turbulent plasmaspheric boundary layer. *Geophysical Research Letters*, *37*, L07106. https://doi.org/10.1029/2010GL042929

Miura, A., & Sato, T. (1980). Numerical simulation of global formation of auroral arcs. *Journal of Geophysical Research*, *85*, 73.

Newell, P. T., & Meng, C.-I. (1987). Low altitude observations of dispersionless substorm plasma injections. *Journal of Geophysical Research*, *92*, 10063.

Nishida, A. (1966). Formation of plasmapouse, or magnetospheric plasma knee, by combined action of magnetospheric convection and plasma escape from the tail. *Journal of Geophysical Research*, *71*, 5669.

Nishimura, Y., Bortnik, J., Li, W., Lyons, L., Donovan, E., Angelopoulos, V., & Mende, S. (2014). Formation of plasmapouse, or magnetospheric plasma knee, by combined action of magnetospheric convection and plasma escape from the tail. *Journal of Geophysical Research: Space Physics*, *119*, 5295. https://doi.org/10.1002/2014JA020029

Pokhotelov, D., Lotko, W., & Streltsov, A. (2002). Effects of the seasonal asymmetry in ionospheric Pedersen conductance on the appearance of discrete aurora. *Geophysical Research Letters*, *29*(10), 1437. https://doi.org/10.1029/2001GL014010

Pokhotelov, O., Pokhotelov, D., Streltsov, A., Khruschev, V., & Parrot, M. (2000). Dispersive ionospheric Alfvén resonator. *Journal of Geophysical Research*, *105*, 7737.

Russell, A., Wright, A., & Streltsov, A. (2013). Production of small-scale Alfvén waves by ionospheric depletion, ionospheric feedback mechanism and phase mixing. *Journal of Geophysical Research: Space Physics*, *118*, 1450–1460. https://doi.org/10.1002/jgra.50168

Samson, J. C., Harrold, B. G., Ruohoniemi, J. M., Greenwald, R. A., & Walker, A. D. M. (1992). Field line resonaces associated with MHD waveguides in the magnetosphere. *Geophysical Research Letters*, *19*, 441.

Sato, T. (1978). A theory of quiet auroral arcs. *Journal of Geophysical Research*, *83*, 1042.

Southwood, D. J. (1974). Some features of field line resonances in the magnetosphere. *Planetary and Space Science*, *22*, 483.

Streltsov, A., Jia, N., Pedersen, T., Frey, H., & Donovan, E. (2012). ULF waves and discrete aurora. *Journal of Geophysical Research*, *117*, A09227. https://doi.org/10.1029/2012JA017644

Streltsov, A. V., & Lotko, W. (1995). Dispersive field line resonances on auroral field lines. *Journal of Geophysical Research*, *100*, 19457.

Streltsov, A., & Lotko, W. (2004). Multiscale electrodynamics of the ionosphere-magnetosphere system. *Journal of Geophysical Research*, *109*, A09214. https://doi.org/10.1029/2004JA010457

Streltsov, A., & Lotko, W. (2005). Ultra-low-frequency electrodynamics of the magnetosphere-ionosphere interaction. *Journal of Geophysical Research*, *110*, A08203. https://doi.org/10.1029/2004JA010764

Sydorenko, D., & Rankin, R. (2017). The stabilizing effect of collision-induced velocity shear on the ionospheric feedback instability in Earth's magnetosphere. *Geophysical Research Letters*, *44*, 6535. https://doi.org/10.1002/2017GL073415

Titheridge, J. (2003). Ionization below the night F2 layer — A global model. *Journal of Atmospheric and Solar - Terrestrial Physics*, *65*, 1035. https://doi.org/10.1016/S1364-6826(03)00136-6

Trakhtengertz, V., & Feldstein, A. (1981). Influence of Alfvén velocity inhomogeneous profile on magnetospheric convection stratification. *Geomagnetism and Aeronomy*, *21*, 951.

Trakhtengertz, V. Y., & Feldstein, A. Y. (1984). Quiet auroral arcs: Ionospheric effect of magnetospheric convection stratification. *Planetary and Space Science*, *32*, 127.

Trakhtengertz, V., & Feldstein, A. (1991). Turbulent Alfvén boundary layer in the polar ionosphere. 1. Excitation conditions and energetics. *Journal of Geophysical Research*, *96*, 19363.

Voitcu, G., & Echim, M. (2016). Transport and entry of plasma clouds/jets across transverse magnetic discontinuities: Three-dimensional electromagnetic particle-in-cell simulations. *Journal of Geophysical Research: Space Physics*, *121*, 4343–4361. https://doi.org/10.1002/2015JA021973

Watanabe, T., Oya, H., Watanabe, K., & Sato, T. (1993). Comprehensive simulation study on local and global development of auroral arcs and field-aligned potentials. *Journal of Geophysical Research*, *98*, 21391.